RSC Advances

PAPER

View Article Online
View Journal | View Issue

Cite this: *RSC Adv.*, 2022, **12**, 20628

Construction of a novel two-dimensional $AgBiO_3$/BiOBr step-scheme heterojunction for enhanced broad-spectrum photocatalytic performance†

Jianhong Lu,[a] Junhong Bie,[a] Shuai Fu,*[b] Jiaqi Wu,[a] Qiang Huang,[b] Pengli He,[b] Zhe Yang,[b] Xiuji Zhang,[b] Huijie Zhu[ab] and Peiyuan Deng[c]

Efficient S-scheme heterojunction photocatalysts were prepared through *in situ* growth of $AgBiO_3$ on BiOBr. The self-assembled hierarchical structure of $AgBiO_3$/BiOBr was formed from flower-like $AgBiO_3$ and plate-like BiOBr. The optimized $AgBiO_3$/BiOBr heterojunction possessed excellent visible-light photocatalytic degradation efficiency (83%) for ciprofloxacin (CIP) after 120 min, with 1.46- and 4.15-times higher activity than pure $AgBiO_3$ and BiOBr, respectively. Furthermore, the removal ratio of multiple organic pollutants including tetracycline, Rhodamine B, Lanasol Red 5B and methyl orange was also investigated. Environmental interference experiments demonstrated that high pollutant concentrations, low photocatalyst dose and the addition of ions (SO_4^{2-}, PO_4^{3-}, HPO_4^{2-}, $H_2PO_4^-$) inhibited the photocatalytic activities. Subsequently, a simultaneous degradation experiment showed the competitive actions between CIP and RhB for radicals, decreasing the photocatalytic activity of CIP. Furthermore, trapping and electron spin resonance experiments showed that h^+ and $^{\cdot}O_2^-$ played a certain role in the degradation process and that $^{\cdot}OH$ acted as assistant.

Received 19th May 2022
Accepted 9th July 2022

DOI: 10.1039/d2ra03157d

rsc.li/rsc-advances

1 Introduction

As society has progressed, domestic sewage and industrial wastewater have had an extremely significant impact on human health and the environment, which has attracted widespread attention.[1–5] Recently, photocatalytic removal of organic matter and reduction in the amount of heavy metals has been developed as reliable ways to mediate waste using solar irradiation.[6,7] Because visible light comprises ~46% of the energy of the solar spectrum, it is highly desired to develop a visible-light responsive photocatalyst with a narrow bandgap.[8,9]

Bi-based photocatalysts such as $BiVO_4$,[10,11] Bi_2WO_6,[12] Bi_2MoO_6,[13] Bi_2S_3 (ref. 14) and Bi_2O_3 (ref. 15) have received widespread attention because they possess suitable structures. For example, bismuth bromide oxide (BiOBr) has a layered structure characterized by $[Bi_2O_2]^{2+}$ slabs interleaved with double slabs of Br atoms.[16,17] This exceptional structure is helpful for the absorbing activity of visible light and charge-separation of the photogenerated carriers. However, BiOBr possesses common problems like most semiconductor materials including poor light absorptivity and high recombination efficiency.[18,19] To overcome these issues, new synthesis methods have been employed. For example, Zhang prepared ultra-thin BiOBr nano-roundels in water-in-oil emulsion microspheres by a solvothermal route, which results in materials with excellent photocatalytic activity, and the degradation rate of organics reached as high as 99.2%.[20] Liu fabricated a novel n–n type BiOBr/Bi_2WO_6 composite photocatalyst by a one-step solvothermal approach. Photocatalytic degradation experiments revealed that BiOBr–Bi_2WO_6 = 8 : 1 demonstrated excellent tetracycline (TC) degradation (96%) within 120 min.[21] Zou fabricated a novel BiOBr/$FeWO_4$ composite photocatalyst *via* a solvothermal approach. The BiOBr/$FeWO_4$ (4 : 1) showed excellent photocatalytic degradation activity (90%) after 1 h toward doxycycline due to the inhibition of recombination of photo-induced electrons and holes and the improvement of the light response range.[22]

The development of Bi-based $MBiO_3$ (M = Li, Na, Ba, Ca) materials is an exciting area of research in heterogeneous photocatalysis because of the structural variability and excellent physical and chemical properties of these materials.[23] Most M elements are alkaline metals, and the $MBiO_3$-based structures usually have simple preparation methods, mild operating conditions and high product purity. Moreover, insoluble compounds will not cause new problems to the environment. Silver bismuthate ($AgBiO_3$) has a narrow band-gap, effectively

[a]*School of Environmental and Municipal Engineering, North China University of Water Resources and Electric Power, Zhengzhou 450046, Henan, China. E-mail: shuaifu16@163.com*

[b]*Henan International Joint Laboratory of New Civil Engineering Structure, College of Civil Engineering, Luoyang Institute of Science and Technology, Luoyang 471023, Henan, PR China*

[c]*Henan Engineering Research Center of Bird-related Outage, Zhengzhou Normal University, Zhengzhou 450044, Henan, China*

† Electronic supplementary information (ESI) available. See https://doi.org/10.1039/d2ra03157d

absorbing visible light.[24,25] Nevertheless, the narrower band-gap often leads to faster recombination of photo-induced electron/hole pairs. Thus, pure $AgBiO_3$ usually exhibits a relatively poor photocatalytic activity.

To overcome these drawbacks and elevate photocatalytic performance, heterostructure construction with other semiconductors aiming to improve charge transfer efficiency has been widely studied.[26,27] Shen prepared flower-like $AgBiO_3$ loaded on GO/NCDs, which exhibited significantly enhanced degradation activities towards organic pollutants.[28] Wu synthesized a novel binary $AgBiO_3$/g-C_3N_4 composite *via in situ* growth of $AgBiO_3$ on g-C_3N_4, which exhibited improved degradation performance towards organic pollutants of methyl orange (MO), tetracycline (TC), and phenol.[29] More recently, a new step-scheme heterojunction (S-scheme heterojunction) concept was proposed by Yu *et al.*[30] This structure induces the migration of the photo-induced electrons and holes and preserves their redox ability under the influence of an internal electric field due to the differences of the Fermi level of each semiconductor. Wang synthesized S-scheme Sb_2WO_6/BiOBr photocatalysts *via* a precipitation–deposition method, which exhibited enhanced photocatalytic performance compared with pure Sb_2WO_6 and BiOBr for removal of NO.[31] The enhanced photocatalytic performance for the Sb_2WO_6/BiOBr composite was attributed to the S-scheme charge transfer path. It is necessary to combine appropriate semiconductors to improve light absorption capacities of materials, and also to improve the separation and transfer of photogenerated electrons and holes for diverse applications.[32,33]

In this manuscript, a novel S-scheme $AgBiO_3$/BiOBr heterojunction was successfully obtained *via* a facile hydrothermal and *in situ* precipitation method. The morphology and optical properties of the materials were systematically investigated. The photocatalytic activities of $AgBiO_3$/BiOBr were tested towards antibiotic ciprofloxacin (CIP) pollutants as a model pollutant under visible-light irradiation. The influences of catalyst dose and initial concentration of CIP on the catalytic performance of $AgBiO_3$/BiOBr were discussed. Additionally, a photocatalytic mechanism was also proposed.

2 Experimental

2.1. Chemicals

Bismuth nitrate pentahydrate ($Bi(NO_3)_3 \cdot 5H_2O$), potassium bromide (KBr), acetic acid (CH_3COOH), silver nitrate ($AgNO_3$), sodium bismuthate ($NaBiO_3$), sodium chloride (NaCl), sodium phosphate ($Na_3PO_4 \cdot 12H_2O$), disodium hydrogen phosphate ($Na_2HPO_4 \cdot 12H_2O$), potassium dihydrogen phosphate (KH_2PO_4), and sodium sulphate (Na_2SO_4) were purchased from Sinopharm Group Co., Ltd. Isopropanol (IPA), disodium ethylenediaminetetraacetic acid (EDTA-2Na), and 1,4-benzoquinone (BQ) were acquired from Aladdin Reagent Co., Ltd.

All chemicals used were analytical grade reagents and were used without further purification.

2.2. Synthesis of BiOBr nanosheets

The BiOBr nanosheets were obtained by a solvothermal method. Generally, 1.587 g of $Bi(NO_3)_3 \cdot 5H_2O$ were first added to a 200 mL flask containing a mixed solution of 35 mL of deionized (DI) water and 5 mL of acetic acid. Separately, 0.389 g of KBr was dissolved in 30 mL of DI water. Then the KBr solution was added dropwise to the first solution and stirred for 1 h. The reaction mixture was subsequently transferred to a 100 mL Teflon-lined autoclave and heated at 160 °C for 12 h. After heating, the samples were cooled to room temperature. The samples were then washed three times with DI water and absolute ethanol successively, and then dried at 60 °C for 12 h.

2.3. Synthesis of $AgBiO_3$/BiOBr composite

A certain amount of BiOBr powder was added into 50 mL of DI water and sonicated for 10 min. 0.5 mmol $AgNO_3$ was subsequently added. After 30 minutes of additional sonication, 0.5 mmol of $NaBiO_3$ was added to the above solution and stirred for 15 min at 25 °C. After that, the mixture was centrifuged at 5500 rpm. Then the final product was washed three times with DI water and ethanol and dried in a vacuum oven at 60 °C for 24 h. The mass ratio of $AgBiO_3$ and BiOBr were 1 : 1, 1 : 5, 1 : 10 and 1 : 15, which are referred to AB-1, AB-5, AB-10 and AB-15, throughout this manuscript. Pristine $AgBiO_3$ was prepared *via*

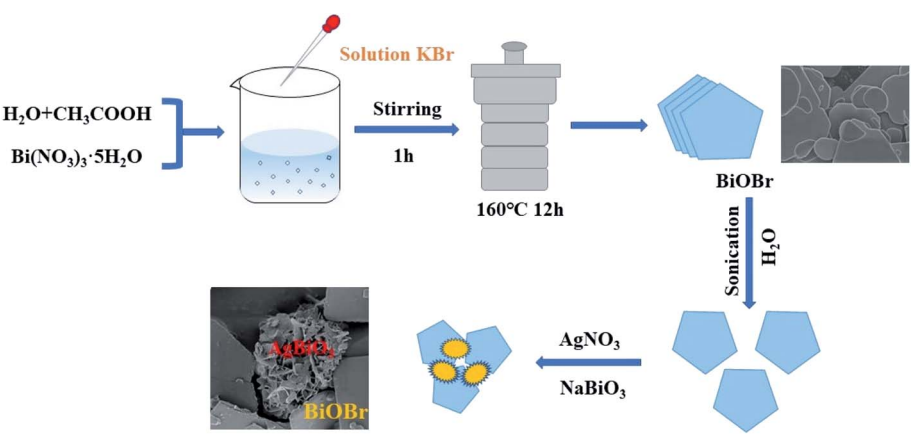

Scheme 1 Schematic of the *in situ* fabrication of the $AgBiO_3$/BiOBr heterojunction.

similar procedures without adding BiOBr. The preparation process of $AgBiO_3$/BiOBr composite is described in Scheme 1.

2.4. Characterization

The morphology of $AgBiO_3$/BiOBr was investigated by high-resolution transmission electron microscopy (HRTEM, JEM-2100, Japan) and scanning electron microscopy (SEM, SU8010, Japan) equipped with energy dispersive spectroscopy (EDS). Zeta potential were measured by a Malvern Zetasizer instrument (Zetasizer Nano Zs, Britain). The X-ray diffraction (XRD) patterns of $AgBiO_3$/BiOBr heterojunctions were collected with a Bruker D8 Advance diffractometer using Cu Kα radiation (λ = 0.15406 nm) at 2θ ranging between 10° and 80°. The specific surface areas of the $AgBiO_3$/BiOBr heterojunctions were evaluated using N_2 adsorption isotherm on a Gemini-2380 (Quantachrome) system. The UV-vis diffuse reflection spectra were measured using a Lambda 950 UV-vis spectrophotometer. A Pick Quant FLuo Time 300 spectrometer was used to collect the steady-state photoluminescence (PL) spectra of the samples. The structures of the $AgBiO_3$/BiOBr samples were also characterized with X-ray photoelectron spectroscopy (XPS, ESCALAB 250Xi). The electron spin resonance (ESR) spectra were measured on a Bruker ER300-SRC instrument.

2.5. Evaluation of visible-light-driven photocatalytic performance

The photocatalytic activities of the $AgBiO_3$/BiOBr samples were evaluated by degradation of CIP in an aqueous solution under visible-light irradiation (350 W Xe lamp with a UV-cutoff filter, λ > 420 nm). The photocatalysts (40 mg) were dispersed in CIP solution (40 mL at a concentration of 20 mg L^{-1}). The suspensions were stirred magnetically for 30 min in the dark to confirm adsorption–desorption equilibrium prior to irradiation. As the reaction proceeded, an aliquot (3 mL) was gathered at various times and centrifuged to remove the photocatalyst for UV-vis measurements (UV-2450) at the maximum absorption wavelength of 273 nm for CIP.

3 Results and discussion

3.1. Physicochemical properties

The XRD patterns of the samples are depicted in Fig. 2. For bare BiOBr, all of the diffraction peaks can be well indexed to the tetragonal phase of JCPDS card no. 09-0393.[34] The diffraction peaks at 19.0°, 21.3°, 28.7°, 31.7°, 35.9°, 46.7° and 57.5° are assigned to the (101), (012), (104), (110), (113), (116), and (215) crystal planes, respectively. These assignments are consistent with the standard diffraction patterns of $AgBiO_3$ (JCPDS 89-9072).[29] For the $AgBiO_3$/BiOBr heterojunction, the presence of $AgBiO_3$ does not affect the BiOBr diffraction peak position (Fig. S1†), indicating that $AgBiO_3$ nanoflowers grew on BiOBr nanosheets without any chemical reaction. The peak intensities of the BiOBr (001) and (002) planes decreased as the mass ratio of $AgBiO_3$ to BiOBr increased, indicating that the $AgBiO_3$ affected the orientation of BiOBr growth.

The chemical environment and oxidation state of the elements present on the surface of the as-synthesized samples were investigated using X-ray photoelectron spectroscopy. The XPS spectra of AB-5 heterojunction together with pure $AgBiO_3$ and BiOBr are shown in Fig. 1. As depicted in Fig. 1b, the survey spectrum of AB-5 was composed of Bi, Br, O and Ag. The binding energies at 159.06 eV and 164.36 eV for Bi $4f_{7/2}$ and Bi $4f_{5/2}$ indicate the existence of Bi^{3+} in AB-5 (Fig. 1c).[35] In the Br 3d spectrum, two characteristic peaks at 67.52 eV and 68.92 eV are assigned to Br $3d_{5/2}$ and Br $3d_{3/2}$ of Br^-, respectively (Fig. 1d). From Fig. 1e, it can be seen that the peak of O 1s located at 529.88 eV, which corresponds to lattice oxygen.[36] The peaks at 531.50 eV and 534.03 eV are associated with adsorbed oxygen and surface O–H or H_2O, respectively.[37] In the Ag 3d spectrum of

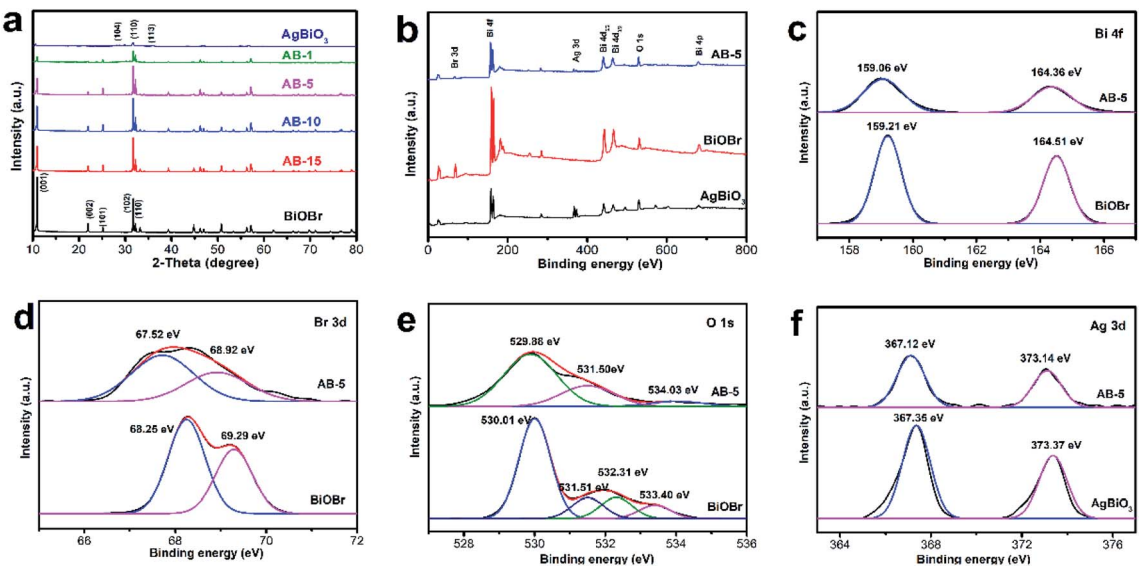

Fig. 1 (a) XRD patterns of as-synthesized samples; XPS spectra of BiOBr, $AgBiO_3$, and AB-5 composite: (b) survey XPS spectra (c) Bi 4f, (d) Br 3d, (e) O 1s, and (f) Ag 3d.

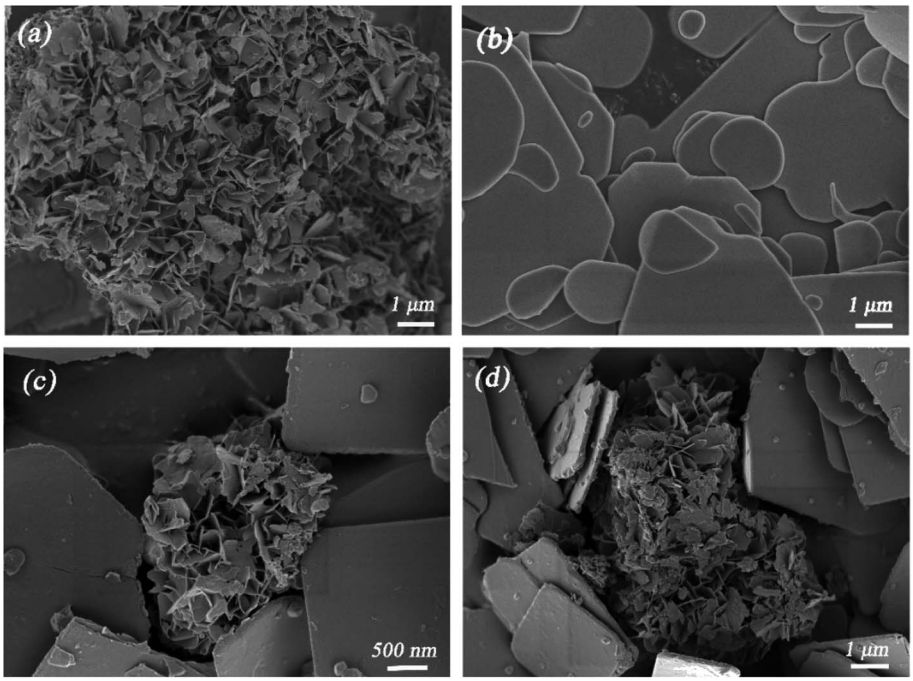

Fig. 2 The SEM image of (a) $AgBiO_3$, (b) BiOBr and (c and d) AB-5 heterojunction.

AB-5 shown in Fig. 1f, the peaks at 367.12 eV and 373.14 eV are ascribed to Ag $3d_{5/2}$ and Ag $3d_{3/2}$, respectively. These peaks demonstrate the existence of Ag^+ in the composite.[25] The binding energies of Bi 4f, Br 3d, O1s, and Ag 3d for the AB-5 heterojunction all exhibited a negative shift compared with those of pure BiOBr and $AgBiO_3$. These simultaneous shifts are likely due to strong electronic interactions between BiOBr and $AgBiO_3$.

Fig. 2a reveals that pure $AgBiO_3$ possesses as flower-like structure composed of nanosheets with diameters around 600 nm. On the other hand, BiOBr exhibits a plate-like morphology (Fig. 2b). Both $AgBiO_3$ and BiOBr have analogous plate-like structures and interactions due to van der Waals forces, which facilitates and stabilizes $AgBiO_3$ over the BiOBr surface and results in the formation of a tight $AgBiO_3$/BiOBr junction. After the deposition of $AgBiO_3$, the flower-like semiconductor was inserted into disordered plate-like BiOBr, whereas the outer surfaces of BiOBr became rough (Fig. 2c and d).

TEM imaging (Fig. 3a) verifies that the flower-like $AgBiO_3$ was successfully loaded on the surface of the plate-like BiOBr. The corresponding magnified HRTEM image (Fig. 3b) exhibits distinct lattice fringes of 0.276 nm and 0.310 nm in accordance with the (110) plane of BiOBr and (104) plane of $AgBiO_3$, respectively. The EDS elemental mapping indicates that Br, Bi, O and Ag are uniformly distributed at the surface of the AB-5 heterojunction (Fig. 4), further confirming that the as-synthesized composite contains $AgBiO_3$ and BiOBr.

The data in Fig. 5 demonstrates that the as-synthesized samples show a classical IV isotherm, suggesting that the material contains mesoporous. The measured S_{BET} values of BiOBr, $AgBiO_3$ and AB-5 heterojunction were 2.53, 20.99 and 5.78 $m^2\ g^{-1}$, respectively. The surface area of AB-5 heterojunction was almost two times higher than that of BiOBr, suggesting that the introduction of $AgBiO_3$ improves the specific surface area of the materials. For the AB-5 heterojunction, the pore size distribution curve exhibits a sharp peak at 1.2–3.0 nm

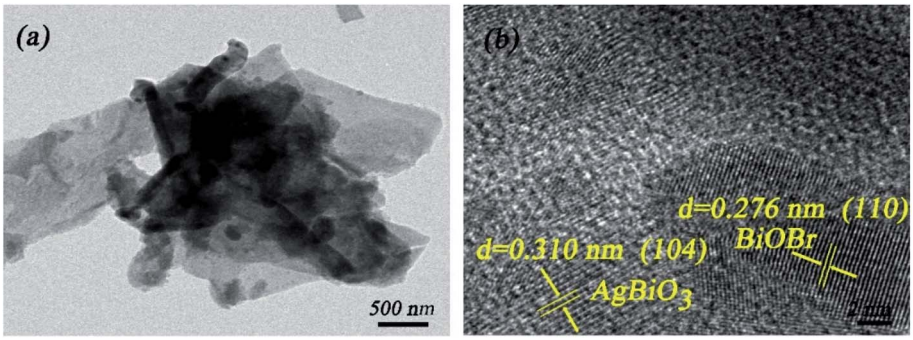

Fig. 3 The TEM image (a) and HRTEM image (b) of AB-5 heterojunction.

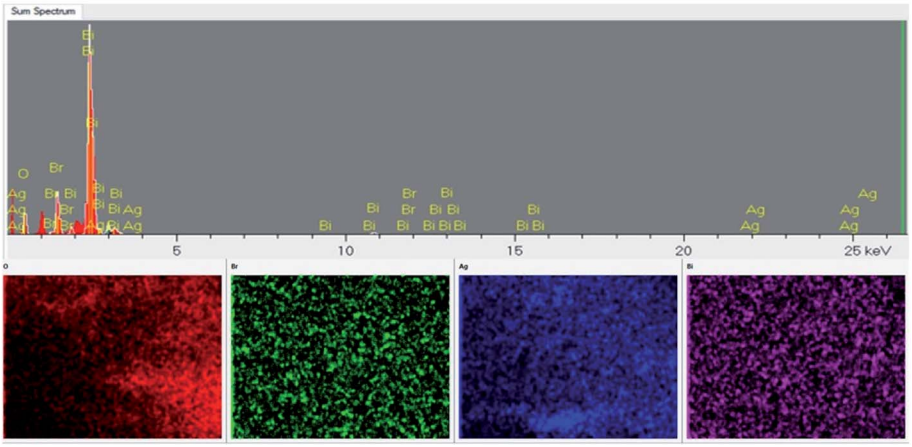

Fig. 4 EDS elemental mapping of AB-5 heterojunction.

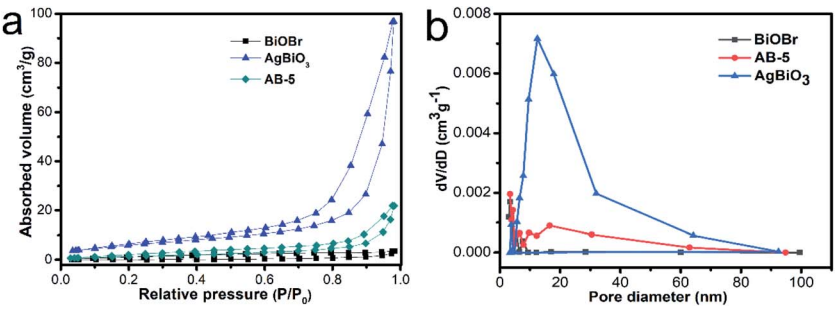

Fig. 5 N_2 adsorption–desorption isotherms and the corresponding pore volume.

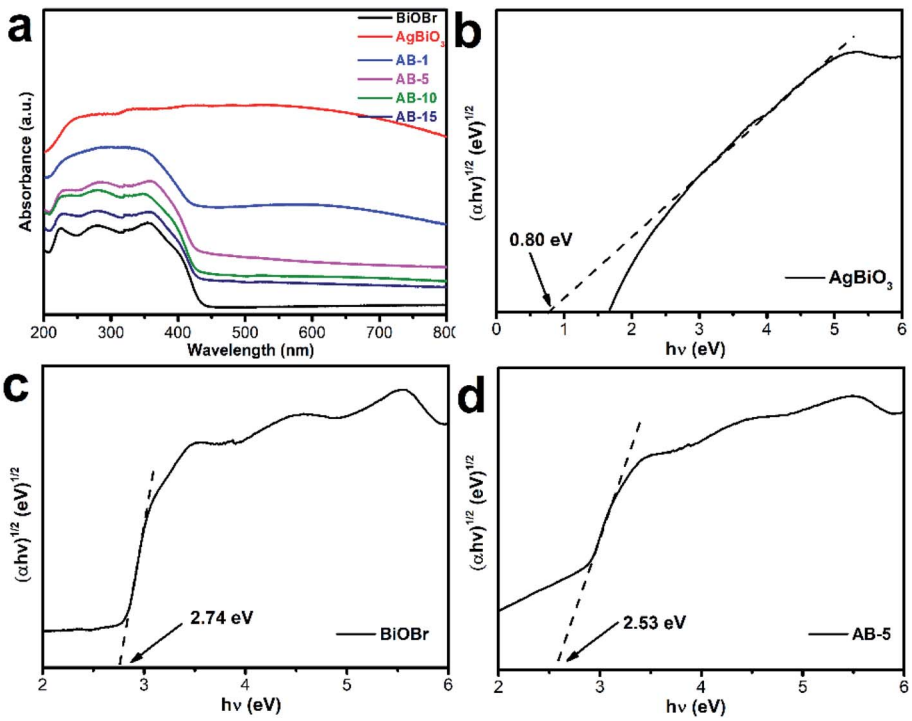

Fig. 6 (a) UV-vis spectra of the as-prepared samples; (b–d) the band gaps of $AgBiO_3$, BiOBr and AB-5 heterojunction.

and a very broad peak at 10–30 nm, together which are indicative of a mesoporous structure. The higher specific surface area and the porous structure of AB-5 heterojunction effectively promote the kinetics of photocatalytic reaction due to the increase number of active sites.[38]

The as-synthesized photocatalysts were studied by UV-Vis diffuse reflectance spectroscopy to investigate their optical properties (Fig. 6a). The absorption edges of BiOBr are located at 442 nm, while $AgBiO_3$ possesses intense absorption between 200–800 nm. Compared to BiOBr, the absorption band edge of the $AgBiO_3$/BiOBr heterojunction shows a distinct red shift, indicating that $AgBiO_3$ improves visible-light absorption capacity. This result might contribute to the enhanced production of photogenerated electron–hole pairs. The bandgap of the samples was calculated by the Tauc equation as follows eqn (1).

$$\alpha h\nu = A(h\nu - E_g)^{n/2} \quad (1)$$

where α, h, ν, A, and E_g are the optical absorption coefficient, Planck constant, photon frequency, a constant and band gap energy, respectively. In addition, the electronic transitions adhere to the n value: direct-allowed or indirect-allowed transitions for $n = 1$ or $n = 4$, respectively. Because BiOBr[39] and $AgBiO_3$ (ref. 24) are both indirect-allowed semiconductors, E_g can be computed from the plot of $(\alpha h\nu)^{1/2}$ as a function of $h\nu$.[39] As shown in Fig. 6b–d, BiOBr, $AgBiO_3$ and AB-5 heterojunction bandgaps were computed to be 2.74 eV, 0.80 eV and 2.53 eV, respectively.

Fig. 7 displays the valence band (VB) position of the samples as evaluated tested by VB-XPS spectra. The VB positions of BiOBr and $AgBiO_3$ were computed to be 2.11 eV and 0.12 eV, respectively. Subsequently, the conduction band (CB) position was computed by the energy band position formula as follows (2):

$$E_{CB} = E_{VB} - E_g \quad (2)$$

The CB positions of BiOBr and $AgBiO_3$ were computed to be −0.63 eV and −0.68 eV, respectively. The energy band potentials of BiOBr and $AgBiO_3$ are depicted in Table 1.

Table 1 Energy band engineering analysis of $AgBiO_3$ and BiOBr

Samples	E_{CB} for NHE[a]/eV	E_{VB} for NHE[a]/eV	E_g/eV
$AgBiO_3$	−0.68	0.12	0.80
BiOBr	−0.63	2.11	2.74

[a] NHE: normal hydrogen electrode.

3.2. Photocatalytic performance

The photocatalytic activities of the as-prepared materials toward CIP in aqueous solutions were evaluated under visible-light irradiation. As shown in Fig. 8a, adsorption experiments were carried out in the dark for 30 min. When irradiated with visible light, the CIP exhibited negligible degradation over time in the absence of the photocatalyst. With the addition of BiOBr and $AgBiO_3$, the degradation efficiencies of CIP reached 20% and 57% after 120 min under visible-light irradiation, respectively. After introducing $AgBiO_3$, the $AgBiO_3$/BiOBr heterojunction (AB-1, AB-5, AB-10, and AB-15) all possessed better photocatalytic activity than that of pure BiOBr with respective efficiencies of 80%, 83%, 65%, and 50%. In particular, AB-5 exhibited the highest degradation efficiency. This result demonstrated that a moderate amount of $AgBiO_3$ could promotes composite degradation efficiency due to formation of heterojunctions at the interface between $AgBiO_3$ and BiOBr, enhancing visible light absorption and separation efficiency of photogenerated carriers. The mechanical mixture of 5 wt% $AgBiO_3$ and BiOBr were also investigated as a control, and it exhibited lower efficiencies than the $AgBiO_3$/BiOBr heterojunction. This lower efficiency is attributed to poor interfacial contact between $AgBiO_3$ and BiOBr during mechanical mixing.

Fig. 8b depicted the reaction kinetics, which were modeled by a pseudo-first-order kinetic model: $\ln(C_0/C_t) = kt$. The rate constants of $AgBiO_3$, BiOBr, the AB-1, AB-5, AB-10, and AB-15 heterojunctions and the mechanical mixture were 0.00550, 0.00204, 0.01344, 0.01497, 0.00798, 0.00555 and 0.00529 min^{-1}, respectively. The rate constants of AB-5 were 2.72 and 7.34 times higher than those of $AgBiO_3$ and BiOBr, respectively, suggesting that a suitable quantity of $AgBiO_3$ improves the photocatalytic performance of $AgBiO_3$/BiOBr.

The effects of different reaction conditions were also investigated. In Fig. 8c, the concentration of CIP solution was

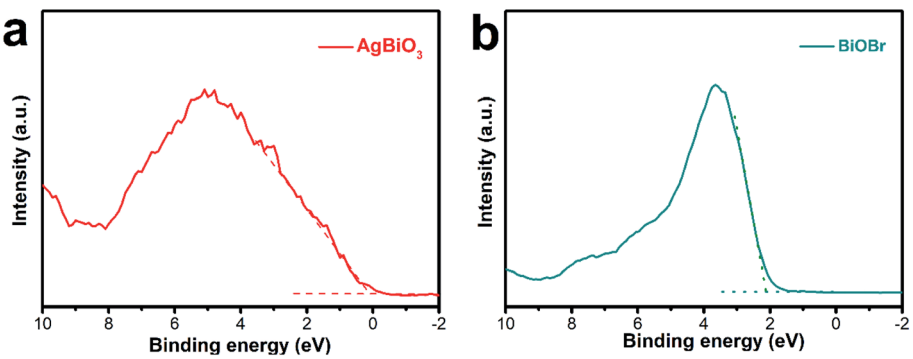

Fig. 7 (a and b) Valence-band XPS spectra of $AgBiO_3$ and BiOBr.

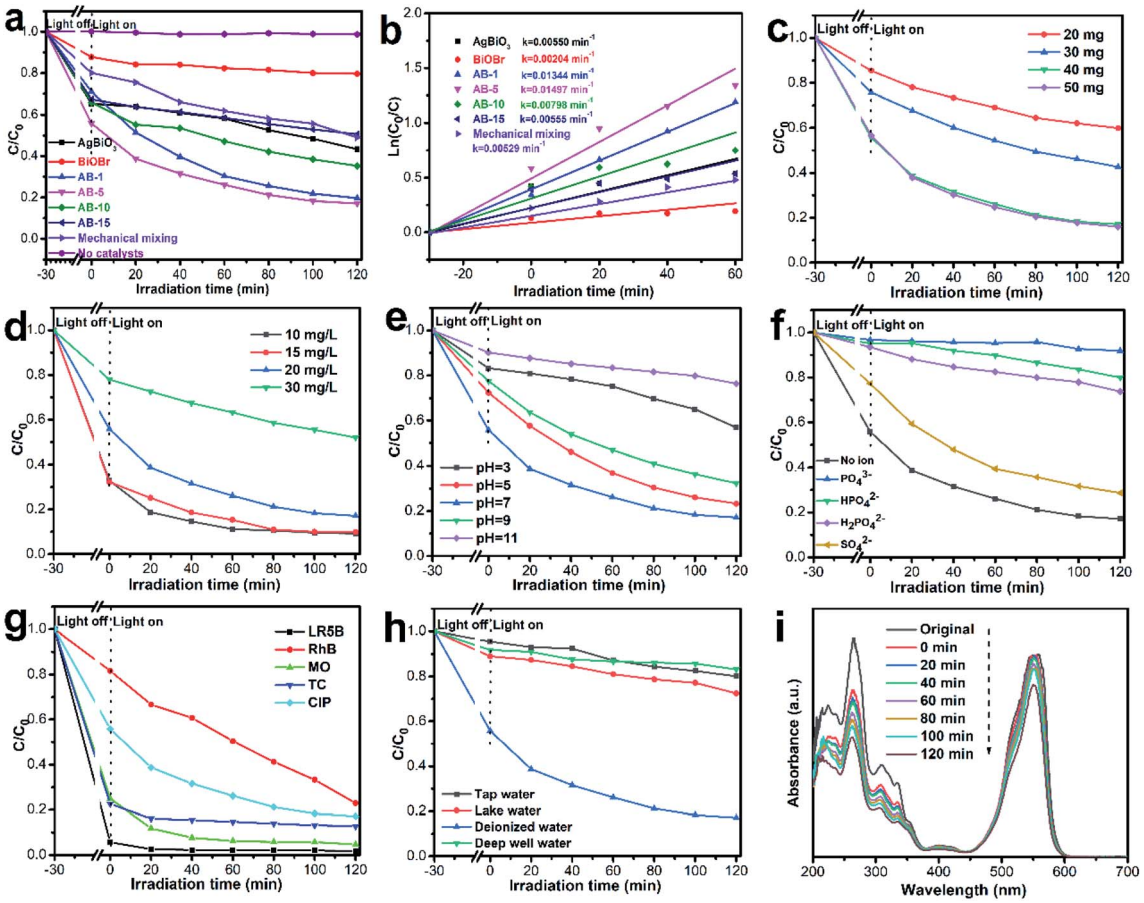

Fig. 8 (a) Degradation efficiencies, (b) the kinetic fit of CIP using the as-prepared photocatalysts under visible-light irradiation; Degradation efficiencies of the CIP solution by (c) various AB-5 dosage ([CIP] = 20 mg L^{-1}), (d) various concentration of CIP ([AB-5] = 40 mg), (e) different pH and (f) under different ion (SO_4^{2-}, PO_4^{3-}, HPO_4^{2-} and $H_2PO_4^{-}$); (g) photodegradation of TC, RhB, LR5B, MO and CIP; (h) degradation efficiency of different solvents in the presence of AB-5; (i) time-dependent absorption spectra of CIP and RhB degradation.

20 mg L^{-1} (pH = 7). When the dosage of AB-5 heterojunction increases from 20 mg to 40 mg, the photocatalytic degradation rate of CIP increases from 40% to 83% after 120 min under visible-light irradiation. The improved photocatalytic activity originates from the greater quantity of active species.[40] However, when the photocatalytic dosage further increases to 50 mg, the degradation rate of CIP is not significantly improved. Therefore, considering the cost of photocatalyst, 40 mg was considered to be optimal for subsequent investigations. As shown in Fig. 8d, the photocatalytic degradation efficiency of CIP was reduced, increasing the initial concentration of CIP. The phenomenon might be because the higher concentration of CIP consumes the generated radicals faster.

Fig. 8e shows that the AB-5 heterojunction exhibits excellent photocatalytic activity at pH 7. At neutral pH, AB-5 and CIP are electroneutral, which allows the CIP molecule to interact with the AB-5. As a result, AB-5 can readily adsorb CIP and show increased photodegradation activity. When the pH is decreased below 6.09, CIP exists its cationic state,[41] which induces electrostatic repulsions between the positively charged surface of AB-5 (Fig. 9) and protonated CIP molecules, which serves to attenuate the adsorption capacity of AB-5.[42] Therefore, at pH values above 7, the photocatalytic activity of AB-5 was significantly decreased. This phenomenon likely occurs because AB-5 undergoes chemical changes under alkaline conditions.

It is widely known that the real wastewaters often contain various inorganic salts, which could affect the efficacy of the

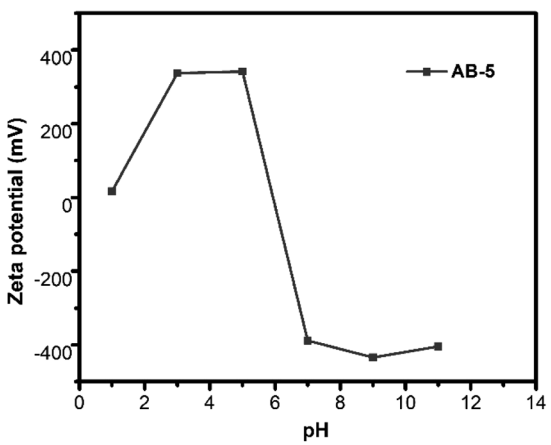

Fig. 9 Zeta potential of AB-5 heterojunction.

pollutant treatment. Therefore, the effect of several common anions in wastewater (SO_4^{2-}, PO_4^{3-}, HPO_4^{2-} and $H_2PO_4^-$) at a concentration of 1 mmol L^{-1} on CIP degradation in the AB-5 system was studied. As shown in Fig. 8f, the addition of SO_4^{2-} slightly affects the degradation efficiency of CIP (72%). This decrease in degradation efficiency might be because SO_4^{2-} consumes $^{\bullet}OH$ to produce $^{\bullet}SO_4^-$,[43,44] thus lowering the degradation rate of CIP. Furthermore, the CIP degradation ratio was significantly reduced in the presence of PO_4^{3-}, HPO_4^{2-} and $H_2PO_4^-$. Compared to HPO_4^{2-} (21%) and $H_2PO_4^-$ (27%), the degradation efficiency of AB-5 towards CIP became almost completely inhibited by PO_4^{3-}, which might be due to the consumption of photogenerated holes by PO_4^{3-}. With the reaction of photo-induced holes, PO_4^{3-} is transformed into HPO_4^{2-}. Similarly, HPO_4^{2-} is changed into $H_2PO_4^-$ after reacting with the photo-induced holes. However, changing PO_4^{3-} into HPO_4^{2-} is more kinetically facile than transforming HPO_4^{2-} into $H_2PO_4^-$. Consequently, the inhibition effect of PO_4^{3-} is stronger than those of HPO_4^{2-} and $H_2PO_4^-$.[45]

To evaluate the range of synthetic materials that can be degraded, several molecules including CIP, TC, LR5B, RhB and MO were investigated. As shown in Fig. 8g, the removal ratios of CIP, TC, LR5B, RhB and MO were 83%, 87%, 98%, 77% and 95%, respectively. The differences in degradation rations are due to each contaminant's distinct molecular structure and adsorption characteristics. Interestingly, we found that the AB-5 had excellent removal efficiencies toward LR5B, MO and TC, depending on adsorption rather than degradation. Moreover, when CIP and RhB coexisted, the mutual effect was investigated (Fig. 8i). The CIP degradation ratio decreased from 83% to 48% in presence of RhB. The reason for this decrease in removal efficiency might be due to competitive interactions for active species between RhB and CIP.[46]

To further understand the photocatalytic applicability of AB-5 in an actual environment, CIP photodegradation in different solvents with AB-5 was investigated. In these experiments, DI water was used as a control. Fig. 8h exhibits the effect of different solvents on the photocatalytic process. When CIP was dissolved in DI water, lake water, tap water and deep well water, the photocatalytic degradation efficiencies were 83%, 28%, 24% and 17%, respectively. The photocatalytic degradation of CIP in environmental waters was significantly inhibited. This phenomenon may be related to inorganic ions and organic pollutants, which could consume the free radicals produced by the AB-5 heterojunction.

3.3. Photocatalytic mechanism

To observe the migration and separation efficiency of the photo-induced charge, PL spectroscopy was performed. Generally, a weaker PL intensity reflects a lower recombination probability. As shown in Fig. 10, With the addition of $AgBiO_3$, the PL intensity of $AgBiO_3$/BiOBr heterojunction (AB-5) decreased compared to pure BiOBr, suggesting that the recombination of charge carriers was inhibited. AB-5 exhibits the effective charge separation efficiency, which is instrumental in improving photocatalytic activity. The electrochemical experiment is

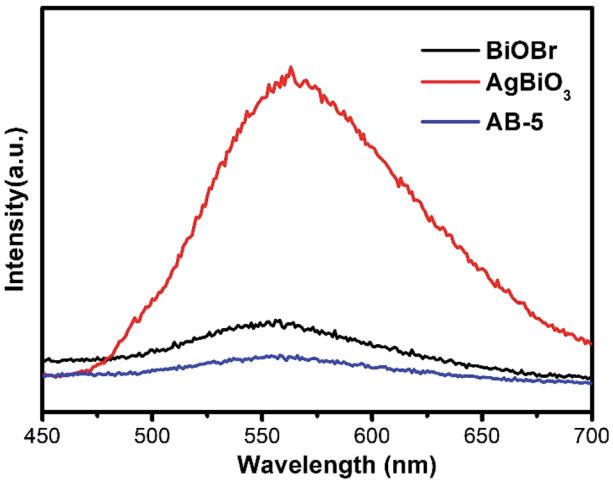

Fig. 10 PL spectra of the as-prepared samples.

conducted to investigate the separation and transfer property of photo-induced electron–hole pairs. As shown in Fig.S3,† AB-5 exhibited the highest photocurrent density *via* switch On/Off under visible light irradiation, indicating that a lower recombination and more rapid charge transfer could be achieved *via* heterostructure.

Trapping experiments were performed to further interrogate the photocatalytic mechanism of CIP degradation. Benzoquinone (BQ), isopropanol (IPA), and disodium ethylenediaminetetraacetate (EDTA-2Na) were used as scavengers for superoxide radicals ($^{\bullet}O_2^-$), hydroxyl radicals ($^{\bullet}OH$), and photo-induced holes (h^+), respectively.[47] Fig. 11a shows the degradation efficiencies of CIP in the presence of various scavengers. Compared to the sample without radical scavenger, the degradation efficiencies of AB-5 toward CIP decreased to 23%, 62%, and 8% upon addition of BQ, IPA, and EDTA-2Na, respectively. These results indicate that the photo-induced holes and superoxide radicals played a critical role in the degradation process, and hydroxyl radicals act as assistants. Additionally, the generation of reactive oxygen species (ROS) using the AB-5 composite was detected using DMPO and TEMPO spin-trapping ESR techniques, which elucidated the degradation mechanism when using the combined pollutants. As shown in Fig. 11b, the strong signal in the dark implied the presence of TEMPO-h^+, which gradually weakened under visible-light irradiation, suggesting that photo-induced holes are the main active species.[48,49] In Fig. 11c and d, the typical signals of DMPO-$^{\bullet}O_2^-$ and DMPO-$^{\bullet}OH$ were tested with the AB-5 composite under visible-light irradiation,[50] suggesting that $^{\bullet}O_2^-$ and $^{\bullet}OH$ radicals emerged during the degradation process.

Based on the above experiment results, the possible estimation of the energy band was conducted. In Fig. 12, under visible-light irradiation electron–hole pairs were induced on the surface of $AgBiO_3$ and BiOBr. According to band structure analysis, the $AgBiO_3$/BiOBr contains a typical II-type heterojunction. Nevertheless, if the composite obeys the II-type heterojunction charge transfer mechanism, the photogenerated holes would accumulate in the VB of $AgBiO_3$ and would not have

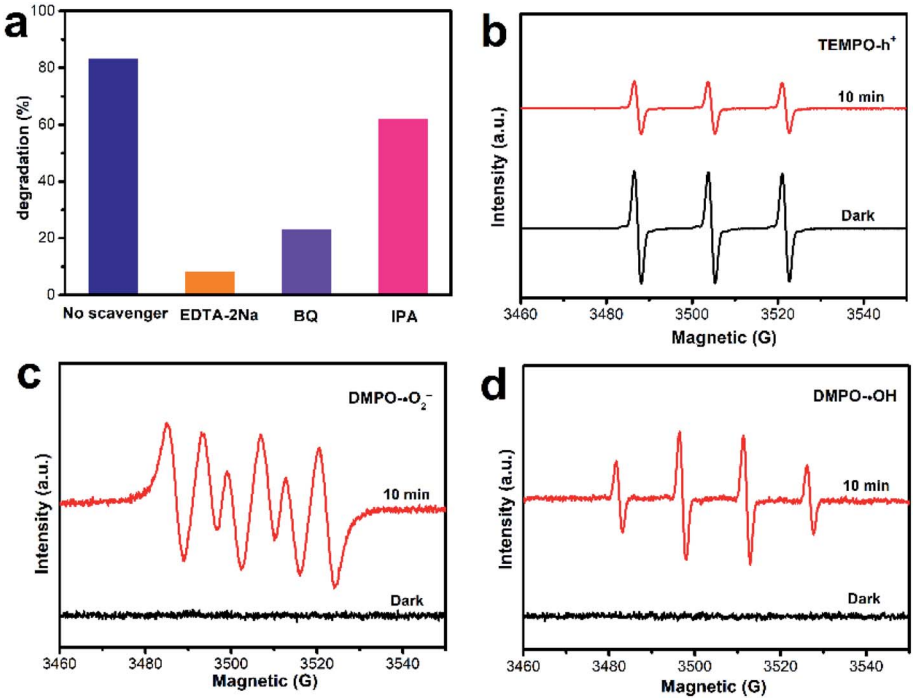

Fig. 11 (a) Trapping experiments of active species during photodegradation of CIP in the presence of AB-5 under visible-light irradiation; (b) TEMPO-h^+, (c) DMPO-$^{\bullet}O_2^-$and (d) DMPO-$^{\bullet}$OH adducts on AB-5 under visible-light irradiation.

a sufficiently high oxidation potential (only 0.12 eV for VB of $AgBiO_3$) to generate $^{\bullet}$OH ($^{\bullet}OH/H_2O$, +1.99 eV).[51] Based on the energy band structure and free radical experiment results discussed above, the S-scheme photocatalytic mechanism is more suitable,[30,52,53] which is formed attributed to the coupling of chemical bonds, the large contact area and the difference of Fermi level between the $AgBiO_3$ and BiOBr molecules. The novel transfer pathways not only promoted the separation of photogenerated carriers and restrained the recombination of electrons and holes, but they also maintained stronger redox ability. The electrons and holes originate from CB of BiOBr and VB of $AgBiO_3$, respectively, which recombine with each other due to the internal electric field and band edge bending interaction. They retain photo-induced charge with higher redox potential. The stacked holes on the VB of BiOBr could react with H_2O to form $^{\bullet}$OH because VB potential was higher than the standard redox potential of $^{\bullet}OH/H_2O$ (+1.99 eV *vs.* NHE). Therefore, the holes and $^{\bullet}$OH directly degrade organic pollutants adsorbed on the AB-5 composite surface. The CB potential edge of $AgBiO_3$ (−0.68 eV *vs.* NHE) efficiently produces $^{\bullet}O_2^-$ (E ($O_2/^{\bullet}O_2^-$) = −0.33 eV *vs.* NHE). Thus, the proposed S-scheme mechanism route of photoinduced carrier charge separation is thermodynamically favorable in the composite.

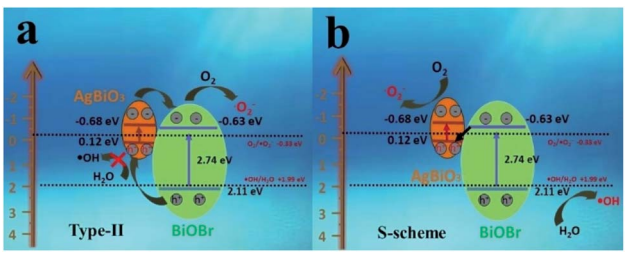

Fig. 12 Proposed photocatalytic mechanism scheme of S-scheme $AgBiO_3$/BiOBr.

4 Conclusions

In this work, S-scheme $AgBiO_3$/BiOBr heterojunctions were designed through a facile hydrothermal and *in situ* precipitation method. XRD, XPS, SEM, TEM and BET characterization methods were systematically utilized to evaluate the morphology of the materials. The optimized $AgBiO_3$/BiOBr heterojunction possesses excellent performance for CIP degradation. The highest photodegradation efficiency of CIP was 83%, which was 1.46- and 4.15-times greater activity than those of pure $AgBiO_3$ and BiOBr, respectively. For other contaminants, the removal efficiencies were 98% (LR5B), 77% (RhB), 87% (TC), and 95% (MO). Environmental interfering experiments demonstrated that low catalyst dose, high CIP concentrations and the addition of ions (SO_4^{2-}, PO_4^{3-}, HPO_4^{2-} and $H_2PO_4^-$) decreased the photocatalytic efficiency. The coupled S-scheme $AgBiO_3$/BiOBr heterojunction achieved enhanced visible-light response, improved the charge separation and suppressed the recombination of electron–hole, and preserved redox ability. Furthermore, an S-scheme mechanism was proposed from trapping experiments and ESR result, indicating that photoinduced holes and superoxide radicals both play a critical role in the degradation process and that hydroxyl radicals acted as assistants.

Author contributions

Jianhong Lu: Conceptualization, Methodology, Software, Investigation, Formal analysis, Writing - original draft, Writing - review & editing. Junhong Bie: Software, Resources, Investigation. Formal analysis. Shuai Fu: Conceptualization, Software, Writing - review & editing, Resources, Visualization, Funding acquisition. Jiaqi Wu: Formal analysis, Data curation, Writing - review & editing. Qiang Huang: Methodology, Software. Pengli He: Investigation, Formal analysis. Zhe Yang: Investigation, Data curation, Funding acquisition. Xiuji Zhang: Investigation, Funding acquisition. Huijie Zhu: Project administration, Supervision. Peiyuan Deng: Conceptualization, Visualization, Funding acquisition.

Data availability statement

All data, models, and code generated or used during the study appear in the submitted article.

Conflicts of interest

There are no conflicts of interest.

Acknowledgements

The support of this work by the National Natural Science Foundation of China (Grant No. 51709141), the Key Science and Technology Research Projects of Henan Province (Grant No. 222102320376) and the Key Scientific Research Project in Universities of Henan Province (Grant No. 22B130001).

References

1 F. Beshkar, O. Amiri and Z. Salehi, Synthesis of $ZnSnO_3$ nanostructures by using novel gelling agents and their application in degradation of textile dye, *Sep. Purif. Technol.*, 2017, **184**, 66–71.

2 J. Zhang, P. Li, X. Zhang, X. Ma and B. Wang, Aluminum metal–organic frameworks with photocatalytic antibacterial activity for autonomous indoor humidity control, *ACS Appl. Mater. Interfaces*, 2020, **12**, 46057–46064.

3 W. Wang, J. Fang and H. Chen, Nano-confined g-C_3N_4 in mesoporous SiO_2 with improved quantum size effect and tunable structure for photocatalytic tetracycline antibiotic degradation, *J. Alloys Compd.*, 2020, **819**, 153064.

4 D. Li, P. Yu, X. Zhou, J. H. Kim, Y. Zhang and P. J. J. Alvarez, Hierarchical $Bi_2O_2CO_3$ wrapped with modified graphene oxide for adsorption-enhanced photocatalytic inactivation of antibiotic resistant bacteria and resistance genes, *Water Res.*, 2020, **184**, 116157.

5 L. Shan, J. Li, Z. Wu, L. Dong, H. Cheng, D. Li and X. Zhang, Unveiling the intrinsic band alignment and robust water oxidation features of hierarchical $BiVO_4$ phase junction, *Chem. Eng. J.*, 2022, **436**, 131516.

6 J. Hu, J. Li, J. Cui, W. An, L. Liu, Y. Liang and W. Cui, Surface oxygen vacancies enriched FeOOH/Bi_2MoO_6 photocatalysis-fenton synergy degradation of organic pollutants, *J. Hazard. Mater.*, 2020, **384**, 121399.

7 X. Zhao, J. Wu, X. Sun, L. You, J. Wu, M. Zhou, Q. Liu, Z. Liu, Y. Qi and R. Wang, Rational design bionic flower-like $BiOBr_{0.5}I_{0.5}/WS_2$ Z-scheme heterojunction for efficient oxidation of Hg0: synergistic effect of facets exposed and intrinsic defects, *Chem. Eng. J.*, 2021, **416**, 129537.

8 F. Yang, X. Yu, Z. Liu, J. Niu, T. Zhang, J. Nie, N. Zhao, J. Li and B. Yao, Preparation of Z-scheme $CuBi_2O_4/Bi_2O_3$ nanocomposites using electrospinning and their enhanced photocatalytic performance, *Mater. Today Commun.*, 2021, **26**, 101735.

9 C. Xu, K. Yan, P. Wang, X. Zhou, T. Zhang, Y. Fu and Q. Yan, $CuBi_2O_4$ and rGO co-modified 3D hierarchical flower-like Bi_5O_7I nanoflakes as Z-scheme heterojunction for enhanced photocatalytic performance, *Sep. Purif. Technol.*, 2021, **257**, 117935.

10 W. Zhao, J. Zhang, F. X. Zhu, F. H. Mu, L. L. Zhang, B. L. Dai, J. M. Xu, A. F. Zhu, C. Sun and D. Y. C. Leung, Study the photocatalytic mechanism of the novel Ag/p-Ag_2O/n-$BiVO_4$ plasmonic photocatalyst for the simultaneous removal of BPA and chromium(VI), *Chem. Eng. J.*, 2019, **361**, 1352–1362.

11 L. Shan, C. Lu and L. Dong, Efficient facet regulation of $BiVO_4$ and its photocatalytic motivation, *J. Alloys Compd.*, 2019, **804**, 385–391.

12 L. Wang, G. Yang, D. Wang, C. Lu, W. Guan, Y. Li, J. Deng and J. Crittenden, Fabrication of the flower-flake-like $CuBi_2O_4/Bi_2WO_6$ heterostructure as efficient visible-light driven photocatalysts: Performance, kinetics and mechanism insight, *Appl. Surf. Sci.*, 2019, **495**, 143521.

13 X. Yang, S. Wang, N. Yang, W. Zhou, P. Wang, K. Jiang, S. Li, H. Song, X. Ding, H. Chen and J. Ye, Oxygen vacancies induced special CO_2 adsorption modes on Bi_2MoO_6 for highly selective conversion to CH_4, *Appl. Catal. B Environ.*, 2019, **259**, 118088.

14 R.-t. Guo, X.-y. Liu, H. Qin, Z.-y. Wang, X. Shi, W.-g. Pan, Z.-g. Fu, J.-y. Tang, P.-y. Jia, Y.-f. Miao and J.-w. Gu, Photocatalytic reduction of CO_2 into CO over nanostructure Bi_2S_3 quantum dots/g-C_3N_4 composites with Z-scheme mechanism, *Appl. Surf. Sci.*, 2020, **500**, 144059.

15 Q. Z. Wang, D. H. Jiao, J. H. Lian, Q. Ma, J. Yu, H. H. Huang, J. B. Zhong and J. Z. Li, Preparation of efficient visible-light-driven $BiOBr/Bi_2O_3$ heterojunction composite with enhanced photocatalytic activities, *J. Alloys Compd.*, 2015, **649**, 474–482.

16 X. Shi, P. Wang, L. Wang, Y. Bai, H. Xie, Y. Zhou and L. Ye, Change in photocatalytic NO removal mechanisms of ultrathin BiOBr/BiOI via NO_3^- adsorption, *Appl. Catal. B Environ.*, 2019, **243**, 322–329.

17 A. Kumar, S. K. Sharma, G. Sharma, A. H. Al-Muhtaseb, M. Naushad, A. A. Ghfar and F. J. Stadler, Wide spectral degradation of Norfloxacin by Ag@$BiPO_4$/BiOBr/$BiFeO_3$ nano-assembly: elucidating the photocatalytic mechanism under different light sources, *J. Hazard. Mater.*, 2019, **364**, 429–440.

18 M. Khan, C. S. L. Fung, A. Kumar and I. M. C. Lo, Magnetically separable BiOBr/Fe_3O_4@SiO_2 for visible-light-

driven photocatalytic degradation of ibuprofen: mechanistic investigation and prototype development, *J. Hazard. Mater.*, 2019, **365**, 733–743.

19 Y. Bai, X. Shi, P. Wang, L. Wnag, K. Zhang, Y. Zhou, H. Xie, J. Wang and L. Ye, $BiOBr_xI_{1-x}$/BiOBr heterostructure engineering for efficient molecular oxygen activation, *Chem. Eng. J.*, 2019, **356**, 34–42.

20 Y. Zhang, P. Cao, X. Zhu, B. Li, Y. He, P. Song and R. Wang, Facile construction of BiOBr ultra-thin nano-roundels for dramatically enhancing photocatalytic activity, *J. Environ. Manage.*, 2021, **299**, 113636.

21 K. Liu, H. Zhang, Y. Muhammad, T. Fu, R. Tang, Z. Tong and Y. Wang, Fabrication of n-n isotype BiOBr-Bi_2WO_6 heterojunctions by inserting Bi_2WO_6 nanosheets onto BiOBr microsphere for the superior photocatalytic degradation of Ciprofloxacin and tetracycline, *Sep. Purif. Technol.*, 2021, **274**, 118992.

22 J. Gao, Y. Gao, Z. Sui, Z. Dong, S. Wang and D. Zou, Hydrothermal synthesis of BiOBr/$FeWO_4$ composite photocatalysts and their photocatalytic degradation of doxycycline, *J. Alloys Compd.*, 2018, **732**, 43–51.

23 W.-L. Zhou and Z.-Y. Zhao, Electronic structures of efficient $MBiO_3$ (M= Li, Na, K, Ag) photocatalyst, *Chin. Phys. B*, 2016, **25**, 037102.

24 X. Yu, J. Zhou, Z. Wang and W. Cai, Preparation of visible light-responsive $AgBiO_{(3)}$ bactericide and its control effect on the Microcystis aeruginosa, *J. Photochem. Photobiol., B*, 2010, **101**, 265–270.

25 J. Gong, C. S. Lee, E. J. Kim, J. H. Kim, W. Lee and Y. S. Chang, Self-generation of reactive oxygen species on crystalline $AgBiO_3$ for the oxidative remediation of organic pollutants, *ACS Appl. Mater. Interfaces*, 2017, **9**, 28426–28432.

26 Z. Gao, K. Chen, L. Wang, B. Bai, H. Liu and Q. Wang, Aminated flower-like $ZnIn_2S_4$ coupled with benzoic acid modified g-C_3N_4 nanosheets via covalent bonds for ameliorated photocatalytic hydrogen generation, *Appl. Catal. B Environ.*, 2020, **268**, 118462.

27 M. Zhang, C. Lai, B. Li, D. Huang, G. Zeng, P. Xu, L. Qin, S. Liu, X. Liu, H. Yi, M. Li, C. Chu and Z. Chen, Rational design 2D/2D BiOBr/CDs/g-C_3N_4 Z-scheme heterojunction photocatalyst with carbon dots as solid-state electron mediators for enhanced visible and NIR photocatalytic activity: kinetics, intermediates, and mechanism insight, *J. Catal.*, 2019, **369**, 469–481.

28 X. Yue, X. Miao, X. Shen, Z. Ji, H. Zhou, Y. Sun, K. Xu, G. Zhu, L. Kong, Q. Chen, N. Li and X. He, Flower-like silver bismuthate supported on nitrogen-doped carbon dots modified graphene oxide sheets with excellent degradation activity for organic pollutants, *J. Colloid Interface Sci.*, 2019, **540**, 167–176.

29 W. Wu, C. Xu, X. Shi, J. Zhao, X. An, H. Ma, Y. Tian and H. Zhou, Effective degradation of organic pollutants and reaction mechanism with flower-like $AgBiO_3$/g-C_3N_4 composite, *Colloids Surf., A*, 2020, **599**, 124901.

30 J. Fu, Q. Xu, J. Low, C. Jiang and J. Yu, Ultrathin 2D/2D WO_3/g-C_3N_4 step-scheme H_2-production photocatalyst, *Appl. Catal. B Environ.*, 2019, **243**, 556–565.

31 Y. Wang, K. Wang, J. Wang, X. Wu and G. Zhang, Sb_2WO_6/BiOBr 2D nanocomposite S-scheme photocatalyst for NO removal, *J. Mater. Sci. Technol.*, 2020, **56**, 236–243.

32 Y. Zhang and S.-J. Park, Facile construction of MoO_3@ZIF-8 core-shell nanorods for efficient photoreduction of aqueous Cr (VI), *Appl. Catal. B Environ.*, 2019, **240**, 92–101.

33 Y. Zhang and S.-J. Park, Stabilization of dispersed CuPd bimetallic alloy nanoparticles on ZIF-8 for photoreduction of Cr(VI) in aqueous solution, *Chem. Eng. J.*, 2019, **369**, 353–362.

34 S. Fu, X. Liu, Y. Yan, L. Li, H. Liu, F. Zhao and J. Zhou, Few-layer WS_2 modified BiOBr nanosheets with enhanced broad-spectrum photocatalytic activity towards various pollutants removal, *Sci. Total Environ.*, 2019, **694**, 133756.

35 L. Li, Y. Yan, H. Liu, J. Du, S. Fu, F. Zhao, S.-M. Xu and J. Zhou, Hollow core/shell β-Bi_2O_3@WS_2 p–n heterojunction for efficient photocatalytic degradation of fluoroquinolones: a theoretical and experimental study, *Inorg. Chem. Front.*, 2020, **7**, 1374–1385.

36 M. Zhou, Z. Guo, Q. Song, X. Li and Z. Liu, Improved photoelectrochemical response of $CuWO_4$/BiOI p–n heterojunction embedded with plasmonic Ag nanoparticles, *Chem. Eng. J.*, 2019, **370**, 218–227.

37 S. Zhang, X. Chen and L. Song, Preparation of BiF_3/BiOBr heterojunctions from microwave-assisted method and photocatalytic performances, *J. Hazard. Mater.*, 2019, **367**, 304–315.

38 G. Liao, W. Yao and J. Zuo, Preparation and characterization of zeolite/$TiO_{(2)}$ cement-based composites with excellent photocatalytic performance, *Materials*, 2018, 11.

39 J. X. Xia, J. Di, S. Yin, H. M. Li, H. Xu, L. Xu, H. M. Shu and M. Q. He, Solvothermal synthesis and enhanced visible-light photocatalytic decontamination of bisphenol A (BPA) by g-C_3N_4/BiOBr heterojunctions, *Mater. Sci. Semicond. Process.*, 2014, **24**, 96–103.

40 C. Yu, P. Yang, L. Tie, S. Yang, S. Dong, J. Sun and J. Sun, One-pot fabrication of β-Bi_2O_3@Bi_2S_3 hierarchical hollow spheres with advanced sunlight photocatalytic RhB oxidation and Cr(VI) reduction activities, *Appl. Surf. Sci.*, 2018, **455**, 8–17.

41 P. Wang, Y. L. He and C. H. Huang, Oxidation of fluoroquinolone antibiotics and structurally related amines by chlorine dioxide: Reaction kinetics, product and pathway evaluation, *Water Res.*, 2010, **44**, 5989–5998.

42 H. Zhang, W. Wu, Y. Li, Y. Wang, C. Zhang, W. Zhang, L. Wang and L. Niu, Enhanced photocatalytic degradation of ciprofloxacin using novel C-dot@Nitrogen deficient g-C_3N_4: synergistic effect of nitrogen defects and C-dots, *Appl. Surf. Sci.*, 2019, **465**, 450–458.

43 W.-D. Oh and T.-T. Lim, Design and application of heterogeneous catalysts as peroxydisulfate activator for organics removal: an overview, *Chem. Eng. J.*, 2019, **358**, 110–133.

44 F. Ghanbari and M. Moradi, Application of peroxymonosulfate and its activation methods for degradation of environmental organic pollutants: review, *Chem. Eng. J.*, 2017, **310**, 41–62.

45 C. Lai, M. M. Zhang, B. S. Li, D. L. Huang, G. M. Zeng, L. Qin, X. G. Liu, H. Yi, M. Cheng, L. Li, Z. Chen and L. Chen, Fabrication of CuS/$BiVO_4$ (040) binary heterojunction photocatalysts with enhanced photocatalytic activity for Ciprofloxacin degradation and mechanism insight, *Chem. Eng. J.*, 2019, **358**, 891–902.

46 S. Y. Dong, X. H. Ding, T. Guo, X. P. Yue, X. Han and J. H. Sun, Self-assembled hollow sphere shaped Bi_2WO_6/RGO composites for efficient sunlight-driven photocatalytic degradation of organic pollutants, *Chem. Eng. J.*, 2017, **316**, 778–789.

47 B. S. Li, C. Lai, G. M. Zeng, L. Qin, H. Yi, D. L. Huang, C. Y. Zhou, X. G. Liu, M. Cheng, P. Xu, C. Zhang, F. L. Huang and S. Y. Liu, Facile Hydrothermal Synthesis of Z-Scheme $Bi_2Fe_4O_9$/Bi_2WO_6 Heterojunction Photocatalyst with Enhanced Visible Light Photocatalytic Activity, *ACS Appl. Mater. Interfaces*, 2018, **10**, 18824–18836.

48 F. Chen, Q. Yang, X. M. Li, G. M. Zeng, D. B. Wang, C. G. Niu, J. W. Zhao, H. X. An, T. Xie and Y. C. Deng, Hierarchical assembly of graphene-bridged Ag_3PO_4/Ag/$BiVO_4$ (040) Z-scheme photocatalyst: an efficient, sustainable and heterogeneous catalyst with enhanced visible-light photoactivity towards tetracycline degradation under visible light irradiation, *Appl. Catal. B Environ.*, 2017, **200**, 330–342.

49 H. Xu, J. Xie, W. Jia, G. Wu and Y. Cao, The formation of visible light-driven Ag/Ag_2O photocatalyst with excellent property of photocatalytic activity and photocorrosion inhibition, *J. Colloid Interface Sci.*, 2018, **516**, 511–521.

50 X. Bai, L. Yang, A. Hagfeldt, E. M. J. Johansson and P. K. Jin, D35-TiO_2 nano-crystalline film as a high performance visible-light photocatalyst towards the degradation of bisphenol A, *Chem. Eng. J.*, 2019, **355**, 999–1010.

51 L. Li, Y. Yan, J. Du, S. Fu, H. Liu, F. Zhao and J. Zhou, Glucose-assisted hydrothermal synthesis of plasmonic Bi deposited nested $Bi_2O_{2-x}CO_3$ photocatalysts with enhanced photocatalytic activity, *Colloids Surf., A*, 2019, **583**, 123946.

52 J. Wang, Q. Zhang, F. Deng, X. Luo and D. D. Dionysiou, Rapid toxicity elimination of organic pollutants by the photocatalysis of environment-friendly and magnetically recoverable step-scheme $SnFe_2O_4$/$ZnFe_2O_4$ nano-heterojunctions, *Chem. Eng. J.*, 2020, **379**, 122264.

53 Q. Xu, D. Ma, S. Yang, Z. Tian, B. Cheng and J. Fan, Novel g-C_3N_4/g-C_3N_4 S-scheme isotype heterojunction for improved photocatalytic hydrogen generation, *Appl. Surf. Sci.*, 2019, **495**, 143555.